ACS OMEGA

Article

http://pubs.acs.org/journal/acsodf

Correlations between Oxygen Uptake and Vacancy Concentration in Pr-Doped CeO_2

Anita M. D'Angelo[†] and Alan L. Chaffee*

School of Chemistry, Monash University, 17 Rainforest Walk, Victoria 3800, Australia

Supporting Information

ABSTRACT: The oxygen uptake of a series of Pr–CeO_2 materials was measured using thermogravimetric analysis at 420 and 600 °C, and at both temperatures, 20% Pr–CeO_2 was found to have the highest uptake. The materials were characterized using X-ray diffraction and scanning transmission electron microscopy. Defects in the materials were identified using Raman spectroscopy, and ultraviolet–visible spectroscopy was used to show the presence of Pr cations in the +3 oxidation state. The existence of these species was attributed to be responsible for the ability of the materials to uptake oxygen. Electron energy loss spectroscopy was used to investigate the effect of Pr addition to CeO_2; the Ce M_5/M_4 and O I_B/I_C ratios were calculated to indicate the relative changes in the Ce^{3+} and oxygen vacancy concentration, respectively. There was no observable increase in the Ce^{3+} concentration; however, the oxygen vacancy concentration increased with an increase in the Pr content. Thus, Pr increases the defect concentration and the ability of the materials to uptake oxygen.

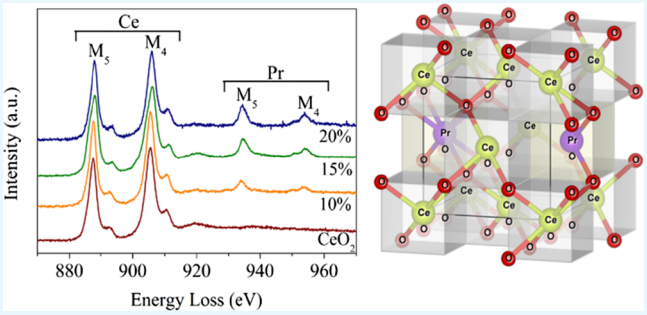

INTRODUCTION

From both an environmental and industrial perspective, the need to develop low-cost oxygen generation technologies is ever-increasing. High-purity (>99%) oxygen is currently generated cryogenically, which requires high energy consumptions, typically of ∼200–220 kW h per tonne of O_2 produced.[1] The energy associated with the air separation unit (ASU) of the plants contributes to the increasing "carbon debt" of the world. Approximately 35% of greenhouse gas emissions arise from energy supply because of the combination of large energy penalties in production and low efficiencies for conversion, transmission, and distribution.[2] Although research has focused on reducing the energy and the associated cost of ASU through the modification of existing systems, sorbent- and membrane-based alternatives have also been proposed as methods of energy reduction.

Applications of CeO_2-based materials as solid oxide fuel cells, catalysts, oxygen sensors, and oxygen separation membranes are driven by the requirements for materials to exhibit both high and reversible oxygen storage capacities (OSC), good electronic and ionic conductivity, and chemical stability and consist of relatively inexpensive components. CeO_2 can reversibly uptake oxygen because of a change in the Ce valence state under redox conditions. Under low partial pressure of oxygen (pO_2) conditions, Ce^{4+} cations are reduced and oxygen is removed from the crystal lattice. Conversely, by increasing pO_2, oxygen migrates into the lattice and Ce^{3+} cations are oxidized. When +3 cations are present, ionic conductivity arises as oxygen ions move toward oxygen vacancies, and electronic conductivity arises from the electron movement by a polaron hopping mechanism.[3] Polaron hopping exhibits a temperature-dependence, in which at higher temperatures electrons are able to move by hopping from Ce^{3+} to Ce^{4+}.[4] In the work by Su et al.,[5] charge transfer on a $CeO_2(111)$ surface with defects was found to occur by polaron migration followed by oxygen diffusion.

The rare-earth cations, Tb and Pr, have been used as dopants to enhance the redox properties of CeO_2. Higher oxygen uptakes are achieved via the formation of extrinsic lattice defects or intrinsically through the removal of oxygen anions from thermal treatment/reduction.[6] The multivalent (+3/+4) nature of Pr and Tb can further enhance the vacancy concentration of CeO_2 and increase both the electronic and ionic conductivities.[7] The increased oxygen uptake of Pr–CeO_2-based materials can be attributed to the variable valence nature and high reducibility of Pr; under a flow of He, Pr^{4+} can be reduced, whereas Ce^{4+} requires a reducing gas such as H_2. During reduction, oxygen is removed from the lattice, generating vacancies and +3 cations that are required to maintain the charge balance of the lattice.[8] At 700 °C, pO_2 of $>10^{-7}$ atm was found to be required for the oxidation of Pr^{3+} in $Ce_{0.8}Pr_{0.2}O_{2-\delta}$.[9] The pO_2 required for the oxidation of Ce^{3+} to Ce^{4+} at room temperature is 10^{-30} atm.[10] High reducibility of the Pr-based materials can also be achieved at temperatures <250 °C.[11] The lower reduction temperature can be attributed to the lower cation reduction energy; 1.83 eV was required to

Received: May 3, 2017
Accepted: May 23, 2017
Published: June 7, 2017

DOI: 10.1021/acsomega.7b00550
ACS Omega 2017, 2, 2544–2551

reduce two Pr^{4+} cations, however, 4.38 eV was needed for the reduction of two Ce^{4+} cations.[12] With the addition of Pr, the reduction energy of CeO_2 decreases twice that of the Pr ionization energy.[13,14] The nonstoichiometry of Pr−Ce oxides varies the reduction enthalpy,[15] and for $Ce_{0.3}Pr_{0.7}O_{2-\delta}$, it has been reported to be 2.9 ± 0.3 eV via Coulometric titration.[16] Chatzichristodoulou and Hendriksen[17] found that the oxygen nonstoichiometry of $Ce_{0.8}Pr_{0.2}O_{2-\delta}$ could be modeled using an excess enthalpic term (ΔH_{Pr}^{exc}) linear in δ (oxygen nonstoichiometry) and defects could be randomly distributed through the lattice. In their work, the reduction behavior of Pr could be described using a δ-linear (nonideal) defect model by estimating the oxidation partial molar enthalpy and entropy. Overall, Pr−CeO_2-mixed oxides have a lower reduction temperature than pure CeO_2 and have a greater oxygen storage and release capacity.[18] Thus, Pr−CeO_2-mixed oxides have been proposed to have applications as oxygen separation materials.

Electron energy loss spectroscopy (EELS) allows for nanometer-length-scale resolution and has been used for the investigation of Pr−CeO_2 materials. Niu et al.[19] reported a decrease in the antibonding Ce peak intensity from the introduction of Pr, evidencing an increase in the Ce^{3+} fraction and an increase in the Ce I_{M_5}/I_{M_4} ratio with increased % Pr. In their work, the Ce I_{M_5}/I_{M_4} ratio of CeO_2 was 0.78, 10% Pr−CeO_2 was 0.82, and 60% Pr−CeO_2 was 1.17. Scanning transmission electron microscopy (STEM)−EELS was used by Rodríguez-Luque et al.[20] to demonstrate the segregation of Pr cations on the surface of CeO_2 particles. Investigations were focused on the Ce edge because of the reducible nature of Pr, which showed the Ce oxidation state varied throughout the particle and that Ce^{3+} was primarily located on the surface. In situ transition electron microscopy (TEM) studies of the reduction process of $Rh/Ce_{0.8}Pr_{0.2}O_2$ catalysts heated under H_2 to 950 °C show that the Ce and Pr edges undergo a 1.4 eV shift to lower energy, the Ce antibonding peak intensities decrease and, for the Pr edge, a peak appears on the lower energy side of the M_4 peak.[21] Furthermore, evidence of oxygen vacancy ordering was first observed at 700 °C, although the reduction of Pr^{4+} occurs below this temperature. The segregation of Gd in CeO_2-based electrolytes has also been evidenced from the integrated intensity ratio of the Gd $N_{5,4}$ and Ce $N_{5,4}$ edges and increased Pr, Gd, and Ce^{3+} concentrations from the respective Pr $M_{5,4}$, Gd $M_{5,4}$, and Ce $M_{5,4}$ edges.[22] Ultrahigh-energy-resolution valence-loss EELS has been used by Bowman et al.[23] to measure the band gap states in $Pr_{0.1}Ce_{0.9}O_{2-\delta}$.

In a similar Tb−CeO_2 system, we have recently reported the qualitative trends between the Ce^{3+} and the oxygen vacancy concentration, % Tb, and oxygen uptake for a series of Tb−CeO_2 materials.[24] This work showed that by increasing the % Tb the oxygen vacancy concentration and the oxygen uptake increased. However, it was also found that there was no observable change in the Ce^{3+} concentration. Here, we have extended this work to report the effect of % Pr on the oxygen uptake, Ce^{3+}, and the oxygen vacancy concentration of CeO_2. To our knowledge, this is the first fundamental study identifying and detailing the correlations between the Pr, defect (oxygen vacancy), and Ce^{3+} concentrations with oxygen uptake. Oxygen uptakes were determined in gas-switching experiments using thermogravimetric analysis (TGA). The materials were characterized using X-ray diffraction (XRD) and STEM. Diffuse reflectance ultraviolet−visible (DR UV−vis) spectroscopy was used to determine the presence of Pr^{3+} cations in CeO_2, which are responsible for oxygen uptake, and Raman spectroscopy was used to determine the existence of vacancy defects. Using EELS, the qualitative relationships between the oxygen uptake and the Ce^{3+} and oxygen vacancy concentration were established.

EXPERIMENTAL SECTION

Material Preparation. The Pr−CeO_2-mixed oxides (Pr = 10, 15, and 20 mol %) were prepared by coprecipitation from $(NH_4)_2Ce(NO_3)_6$ (Aldrich, >98.5%), $Pr(NO_3)\cdot 6H_2O$ (Aldrich, 99.9%), and urea (15× the total ion concentration, Sigma-Aldrich, 99−100.5%), which were dissolved in water and heated at 90 °C for 8 h. $PrO_{2-\delta}$ was prepared using the same conditions with $Pr(NO_3)\cdot 6H_2O$ (Aldrich, 99.9%) and urea. The resultant precipitates were filtered, washed with water and ethanol, and dried overnight in an oven at 100 °C. The materials were heated under a nitrogen atmosphere to 700 °C for 2 h with a heating rate of 2 °C min^{-1}.

X-Ray Diffraction. XRD patterns were collected on a Bruker D8 Focus diffractometer equipped with a monochromatic Cu Kα (λ = 1.5406 Å) source operated at 40 kV and 40 mA. The data were collected over a 2θ range of 5−80, with a step size of 0.02° and a step time of 1° min^{-1}.

Thermogravimetric Analysis. To quantify oxygen uptake, gas-switching experiments were carried out using a Mettler Toledo TGA/DSC 1 system. The samples were weighed (∼10 mg) into an alumina crucible (150 μL) and heated to 420 and 600 °C in a flow of nitrogen (35 mL·min^{-1}) before instrument air was introduced (35 mL·min^{-1}), after which nitrogen was then reintroduced. The flow of air was mixed with a N_2 carrier gas that resulted in a pO_2 of 13.3 kPa delivered to the sample. When the gas was switched to instrument air the weight increase was used to calculate the oxygen uptake. To ensure data consistency, averages were obtained from a minimum of two separate experiments with a maximum of three standard errors of the mean.

Raman Spectroscopy. The spectra were obtained using a Renishaw inVia Raman spectrograph with an excitation wavelength of 632.8 nm from a HeNe source. The spectra were obtained between 2000 and 200 nm, with a spot size of ∼1 μm and a laser power of 1 mW on the sample.

DR UV−Vis Spectroscopy. The presence of Pr^{3+} was identified using a Cary 5000 spectrometer fitted with a DR accessory. The spectra were obtained with a 1 nm data interval between 800 and 200 nm in % reflectance mode with polytetrafluoroethylene as the reference followed by applying the Kubelka−Munk equation.

Transmission Electron Microscopy. STEM bright-field (BF) and high-angle annular dark-field (HAADF) images were obtained at 200 kV on an FEI Tecnai G2 F20 S-TWIN FEGTEM instrument. All samples were prepared by dispersing into butanol and ultrasonicating before dipping an ultrathin holey carbon film into the solution.

EELS measurements were recorded using a JEOL JEM-2100F FEGTEM and Gatan 776 Enfina 1000 parallel detection EELS spectrometer by the method described in D'Angelo et al.[24] The spectra were obtained in diffraction mode using a condenser aperture of 40 μm, a spot size of 1 μm, a dispersion of 0.1 eV/channel, and a collection aperture of 3 mm. Approximately 10 spectra were acquired from different clusters located on the grid with individual crystallites in random orientation. The data were obtained using an acquisition time of 5 s and by summing 20 spectra. These conditions allowed for

DOI: 10.1021/acsomega.7b00550
ACS Omega 2017, 2, 2544−2551

beam damage to be minimized[25] and compositional variations[20] and orientation dependence variation to be eliminated.[26] The background was subtracted using the power-law technique, and the integrated white-line intensities were determined using a 16 eV window for Ce $M_{5,4}$ and a 2 eV window for the O I_B/I_C edge.[27]

RESULTS AND DISCUSSION

Structural and Morphology Characterization. The diffraction patterns of the Pr−CeO_2 materials are presented in Figure 1 and show that all reflections can be indexed to the

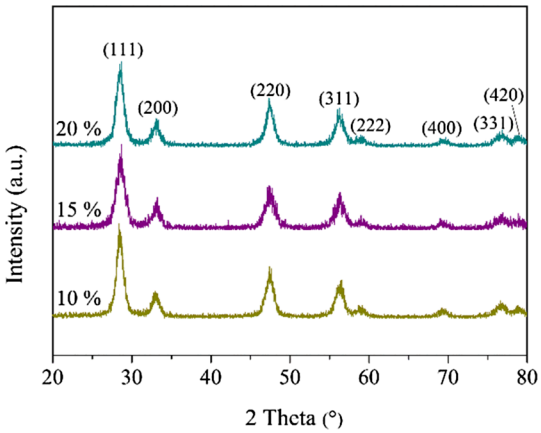

Figure 1. XRD patterns of the Pr−CeO_2-mixed oxides with Pr = 10, 15, and 20% with the reflections from the cubic fluorite structure labeled.

cubic fluorite structure (space group $Fm\bar{3}m$) of CeO_2 (JCPDS card 00-034-0394).[28] Pr−CeO_2-mixed oxides with >20% Pr exhibited phase segregation, as shown in Figure S1; hence, these were not used further in this study.

STEM BF and HAADF images (Figure 2a−c) showed that the materials comprised aggregated crystallites ∼<10 nm. A *d*-spacing of 0.31 nm can be seen for 20% Pr−CeO_2 in Figure 2c, which corresponds to the (111) plane of the CeO_2 cubic fluorite lattice. The images of the synthesized pure $PrO_{2-\delta}$ show that the particles were aggregated and had an elongated octahedral-type morphology (Figure 2d). Further images of the materials are presented in Figure S2.

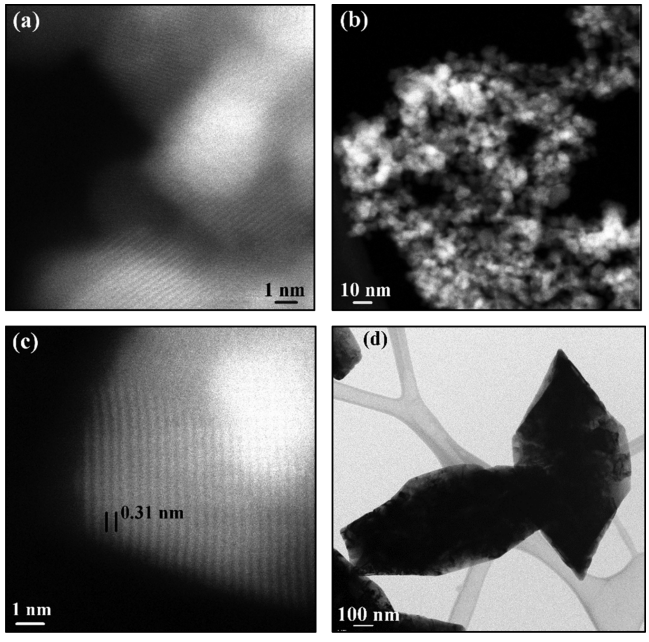

Figure 2. STEM images of the Pr−CeO_2-mixed oxides with Pr = (a) 10, (b) 15, (c) 20%, and (d) pure $PrO_{2-\delta}$.

Measurement of Oxygen Uptake Using TGA. The oxygen uptake of Pr−CeO_2 was measured in gas-switching experiments using TGA, and the results are shown in Figure 3.

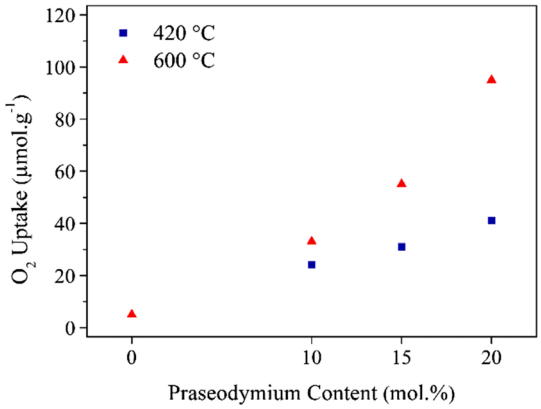

Figure 3. Oxygen uptake of the Pr−CeO_2 oxides at 420 and 600 °C as determined using TGA. CeO_2 had an uptake of <5 μmol·g^{-1}.

The oxygen uptake increased by increasing the % Pr and the analysis temperature. At 420 °C, the uptakes for Pr = 10, 15, and 20% were 24, 31, and 41 μmol·g^{-1}, respectively. In this work, the temperature (420 °C) required for the uptake was comparable with the temperatures used by Mullhaupt[29] for Ce−Pr materials (380−606 °C). Oxygen uptake is considered to be primarily due to the reduction of Pr, in contrast to the reduction of Ce. This is because lower pO_2 (<10^{-30} atm at room temperature) and higher temperatures (>2000 K at ambient pressure) are required to remove oxygen from CeO_2.[10] Oxygen desorption from PrO_2 thin films occurs over the range 377−517 °C as a result of a $PrO_2 \rightarrow Pr_5O_9$ transition.[30] Similarly, the temperature-programmed reduction of Pr_6O_{11} under H_2 showed a main peak at 517 °C, assigned to the maximum amount of bulk oxygen loss.[31] Oxygen vacancies are generated in the crystal structure from the addition of Pr, which increases the ability of the materials to lose oxygen.

Increasing the analysis temperature from 420 to 600 °C resulted in overall increase in the uptake at each % Pr. The uptakes when Pr = 10, 15, and 20% were 33, 55, and 95 μmol·g^{-1}, respectively. These values are significantly higher than the measured uptake of <5 μmol·g^{-1} for CeO_2. Higher uptakes were measured at 600 °C in comparison with those at 420 °C as the materials lose more oxygen when heated, and hence, the extent of reduction is greater. When heating $PrO_{2-\delta}$ under a flow of N_2, a loss of 0.5% at 420 °C and 1.2% at 600 °C is observed and attributed to the loss of oxygen (Figure S3).[8] However, it is considered that weight loss due to the removal of water vapor also contributes to the measured weight loss. Overall, Pr was found to promote the oxygen uptake of CeO_2 at both 420 and 600 °C.

Analysis of Defects Using Raman and DR UV−Vis Spectroscopy. The presence of defects in the Pr-doped CeO_2 materials was determined through Raman spectroscopy and DR UV−vis spectroscopy. A 633 nm Raman excitation laser was

DOI: 10.1021/acsomega.7b00550
ACS Omega 2017, 2, 2544−2551

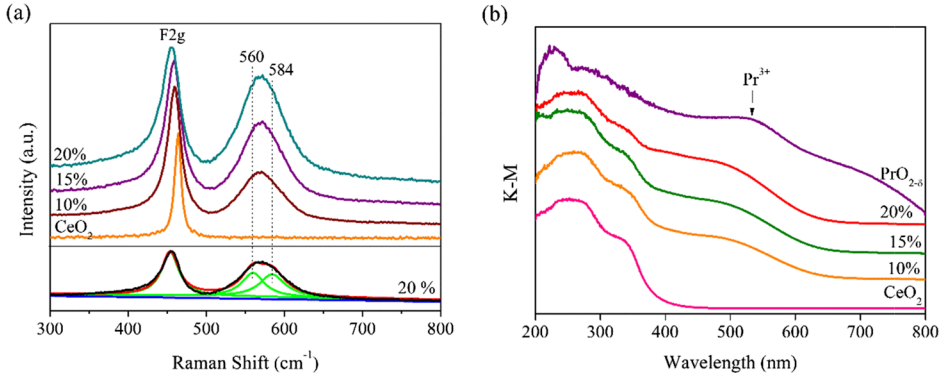

Figure 4. (a) Raman spectra of CeO_2[24] and Pr−CeO_2 with Pr = 10, 15, and 20% showing the defect band characteristic of vacancies. (b) DR UV−vis spectra of CeO_2 and Pr−CeO_2 with Pr = 10, 15, and 20%.

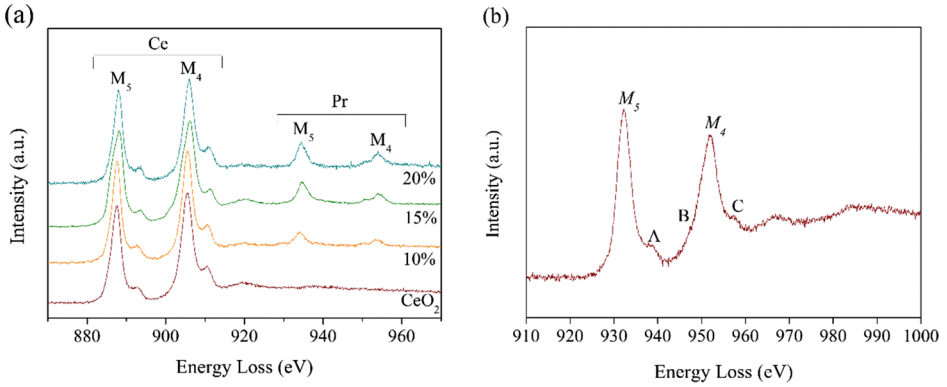

Figure 5. (a) Ce $M_{5,4}$ white lines of CeO_2 and Pr−CeO_2 with % Pr = 10, 15, and 20 and (b) M_5 and M_4 white lines of $PrO_{2-\delta}$.

selected to increase the laser penetration depth and provide bulk and surface information by minimizing optical absorption. Figure 4a shows the presence of an F_{2g} band at 460 cm^{-1} due to a CeO_8-type complex with O_h symmetry and a wide defect band at 500−650 cm^{-1}. As suggested by Li et al.,[32] because of the similar ionic radii of the +3 and +4 Ce and Pr cations, the presence of this defect band is likely from the differences in oxidation states rather than differences in ionic radii. The defect band has been reported to consist of two modes at 560 and 584 cm^{-1} from metal−O complexes both with and without vacancies.[33] Through peak-fitting of the Pr = 20% material spectra using a Lorentzian function, these two species are suggested to be present in the synthesized Pr-doped CeO_2 materials. Defects are introduced into the crystal structure when Pr is added to CeO_2 as this defect mode is not present for CeO_2. For every two +3 cations, one oxygen vacancy is needed to maintain the charge balance of the lattice.

It can also be observed that the F_{2g} band exhibits a downward shift with increasing % Pr. A shift in the F_{2g} mode of the rare-earth-oxide-doped CeO_2 materials has been attributed to the lattice contraction and/or the introduction of vacancies.[34] Lattice contraction may occur by increasing the % Pr as Pr^{4+} (Pr^{4+} = 0.96 Å) cations are smaller (but only slightly) than those of Ce (Ce^{4+} = 0.97 Å).[35] Lee et al.[36] attributed the downward shift in the F_{2g} band of CeO_2 nanorods to volume expansion from the generation of vacancies; the larger the shift, the higher the expected oxygen vacancy concentration. It is predicted that when Pr cations are incorporated into the CeO_2 lattice there is a mixture of Pr in both the +3 and +4 oxidation states. These findings correspond to the understanding that pure $PrO_{2-\delta}$ possesses cations in both the +3 and +4 oxidation states.[37] As the amount of added Pr increases, the concentration of cations in both the +4 and +3 oxidation states is considered to increase. Although vacancies are present in these materials as shown by the defect band at ∼500−650 cm^{-1}, if the concentration of these cations is low, then the lattice may still contract from the increasing amount of Pr^{4+} and result in the F_{2g} mode shift. Ahn et al.[12] reported for a series of Pr-doped CeO_2 using density functional theory (DFT) calculations, that Pr^{3+} was present as the majority ion and Pr^{4+} as the minority ion. The concentration of vacancies and +3 cations is likely not great enough to result in an observable expansion of the lattice cell.

DR UV−vis spectra of CeO_2 and the Pr−CeO_2 materials are presented in Figure 4b. In all spectra, the peak present at ∼250 nm corresponds to Ce^{3+} from a $O^{2-} \rightarrow Ce^{3+}$ charge transfer, the peak at ∼280 nm corresponds to a $O^{2-} \rightarrow Ce^{4+}$ charge transfer, and the peak at ∼330 nm corresponds to an interband transition from the O 2p to Ce 4f band.[38] In addition, a strong absorption is observed between 400 and 650 nm for the Pr−CeO_2 materials because of Pr^{3+} transitions. In the work by Kasprowicz et al.[39] on Pr-doped $Bi_2ZnOB_2O_6$, Pr^{3+} absorption bands between 430 and 490 nm were attributed to $^3H_4$ ground state to ^3P_J transitions and those between 560 and 610 nm from $^3H_4$ to $^1D_2$ transitions. Also, in the work by Strzęp et al.,[40] a prominent 488 nm 4f−4f band was assigned to $^3H_4$ transitions to $^3P_0$ multiplets. It has been reported that Pr^{4+} does not absorb in the UV−vis region.[41,42] Overall, our results show that the Pr−CeO_2 materials contain Pr cations in the +3 oxidation state and oxygen defects/vacancies.

Transition Electron Microscopy−Electron Energy Loss Spectroscopy. TEM−EELS was used qualitatively to

DOI: 10.1021/acsomega.7b00550
ACS Omega 2017, 2, 2544−2551

investigate the relative changes in Ce^{3+} and oxygen concentration of the Pr−CeO_2 materials. The background-subtracted Ce $M_{5,4}$ EELS spectra of CeO_2 and the Pr−CeO_2 materials are presented in Figure 5a and show the presence of two Ce white lines at 883 and 901 eV due to $3d_{5/2} \rightarrow 4f_{7/2}$ (M_5) and $3d_{3/2} \rightarrow 4f_{5/2}$ (M_4) electron transitions, respectively. When Pr is introduced, two Pr $M_{5,4}$ white lines can be observed at 951 and 931 eV that are from 3d to 4f transitions and are characteristic of all lanthanides. The intensity of these peaks increases as the Pr content increases. On the higher energy side of each white line labeled also exists a satellite peak.[43]

The ratio between I_{M_5} and I_{M_4} indicates the f-shell occupancy, where an increase in the number of f-shell electrons results in an increase in the I_{M_5}/I_{M_4} ratio.[44] For pure CeO_2, the intensity of I_{M_5} is less than that of I_{M_4} and all cations are in the +4 oxidation state (Ce^{4+} = $4f^0$). It is expected that the concentration of Ce^{3+} is minimal in CeO_2 because of the low pO_2 required to reduce Ce^{4+}. As the amount of +3 cations increases, that is, electrons in the initial level increase (Ce^{3+} = $4f^1$) and there is a decrease in I_{M4}. For $PrO_{2-\delta}$, as under standard conditions the oxide is nonstoichiometric and consists of cations in both the +3($4f^2$) and +4($4f^1$) states, $I_{M_5} > I_{M_4}$.[45] In Figure 5b, the smaller peaks labeled "A" and "C" on the high-energy side of the M_5/M_4 lines can be observed for $PrO_{2-\delta}$ and are due to Pr^{4+}. A shoulder peak on the lower energy side of M_4, labeled B, from Pr^{3+} is also visible. Here, it is indicated that the cations in $PrO_{2-\delta}$ exist in both the +3 and +4 oxidation states. The two Pr white lines are evident in all of the Pr−CeO_2 materials and show that Pr cations are within the lattice. The Pr ratio for all materials is $I_{M_5} > I_{M_4}$, indicating that a significant portion of the cations is in the +3 oxidation state.

The Ce I_{M_5}/I_{M_4} white-line ratio was calculated for the integrated intensities, and the results are presented in Figure 6

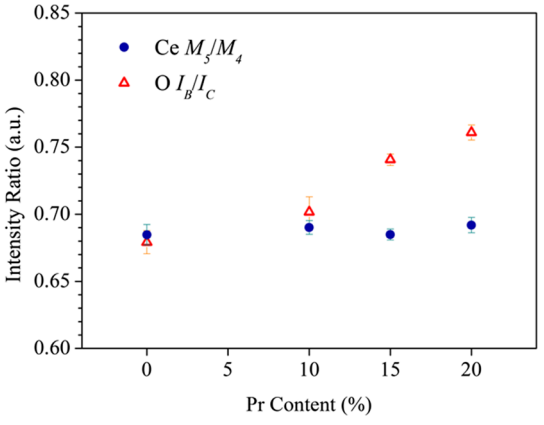

Figure 6. Average Ce I_{M_5}/I_{M_4} and O I_B/I_C intensity ratios for CeO_2 and Pr−CeO_2 with % Pr = 10, 15, and 20.

and Table S1. The Ce I_{M_5}/I_{M_4} ratio for CeO_2 was 0.68 and that for Pr = 10, 15, and 20% was 0.69, 0.68, and 0.69, respectively. Differences between the Ce^{4+}/Ce^{3+} concentrations in these materials are not evident. In our previous work, the Ce I_{M_5}/I_{M_4} ratio for CeO_2 synthesized from a $Ce(NO_3)_3{\cdot}6H_2O$ cerium salt was 0.67 ± 0.01. This result is comparable with the ratio measured in this work for CeO_2, although a different cerium salt was used. A difference in the M_5/M_4 area ratio of 0.01 can correspond to a 9% increase in the amount of Ce^{3+}.[25] It has been reported that using the X-ray absorption near-edge structure, the oxidation state of the Ce cations in Pr−CeO_2 solid solutions does not vary from that of the initial CeO_2 (+4).[19] Furthermore, there is no observable decrease in the Ce and Pr satellite peak intensity as the amount of % Pr increases. Consequently, we interpret the Ce +4/+3 concentration to not vary or at least not significantly or detectably using this method. At higher % Pr, the intensity of the antibonding transitions has been found to decrease for $Ce_{0.9}Pr_{0.1}O_2$ thin films on Si(111) as the amount of Ce^{3+} in the materials increases.[19] As there is no variation in the Ce ratios of the synthesized and Pr−CeO_2 materials or in the intensity of the Ce satellite peaks, the increase in the spectral changes are considered to be due to the introduction of Pr.

The O K (1s) near-edge fine structure spectra of the Pr−CeO_2 materials are presented in Figure 7. The CeO_2 ground

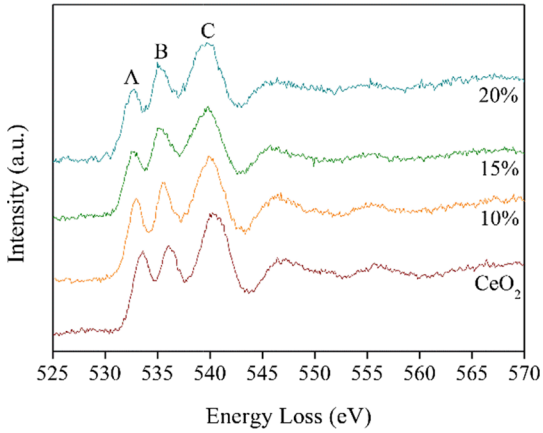

Figure 7. O K (1s) near-edge fine structure of CeO_2 and Pr−CeO_2 with % Pr = 10, 15, and 20.

state has a filled oxygen 2p valence band and, because of the strong hybridization between Ce levels and O 2p orbitals, the electronic structure has been reported to be a mixture of $4f^0$ and $4f^1$−O 2p states.[43,46,47] Because of dipole selection rules, only an s → p transition is permitted; however, this mixing allows for electric dipole transitions from the O 1s orbital to the p-like component of the Ce 4f and 5d states.[48] Similarly, when Pr is added, the mixing of O 2p and Pr 4f states also allows for these transitions.[49,50] The peak labeled "A" arises from O 1s → Ce 4f transitions, and peaks "B" and "C" arise from O 1s → Ce 5d−e_g and 5d−t_{2g} levels in the conduction band, respectively.[51] An increase in the ratio between the peaks labeled B and C has been reported as indicative of the presence of vacancies or defect sites within the crystal lattice. The O I_B/I_C ratio for CeO_2 was 0.68 and that for Pr = 10, 15, and 20% was 0.70, 0.74, and 0.76, respectively. The higher O I_B/I_C ratio for the Pr−CeO_2 materials, compared to CeO_2, shows that the vacancies are generated by the addition of Pr. The vacancies that are generated have been reported to primarily exist around Pr ions rather than Ce.[12] Pr−CeO_2 has a vacancy formation energy of ∼1/3 of CeO_2, which results from both structural and electronic modifications of the lattice.[52] Also, our results reveal that the O I_B/I_C ratio gradually increases with increasing % Pr. This increase was attributed to an increase in the vacancy concentration, which is likely responsible for the observed trend in oxygen uptakes as the % Pr increases.

DOI: 10.1021/acsomega.7b00550
ACS Omega 2017, 2, 2544−2551

Visual inspection of the O K (1s) fine structure shows that the peaks of the 20% Pr−CeO_2 are slightly less defined and broader in comparison to those of CeO_2. In ZnO nanocrystals, Zn L_3 broadening and a weakened fine structure have been reported to be due to an increase in the vacancy concentration.[53] Furthermore, the intensity of the peak labeled A appears to decrease relative to the peak labeled B with increasing % Pr. A decrease in the O I_A/I_C ratio for the Pr−CeO_2 materials compared to CeO_2 may be attributed to an increase in +3 cations filling the 4f state and inhibiting transitions. For CeO_2-based materials consisting of only +3 cations, this peak is not present as the 4f orbital is occupied ($4f^1$).[48] The structure can also be modified to result in the degradation of O 2p−Ce 4f hybridization and a decrease in the intensity of A.[54] Distortion of the crystal lattice occurs as the introduction of Pr^{4+}/Pr^{3+} cations weakens the metal−oxygen bonds, lowering the reduction temperature and ease at which oxygen can be removed. The local structure near the vacancy is distorted as the lattice accommodates the larger Pr^{3+} cations that are generated during reduction.[12] As the material is reduced and +3 cations/vacancies are generated, the resulting structural distortions can result in the broadening of the observed peak.[25] An increase in vacancies and broadened O-extended fine structure have also been observed for vacancy concentrations of ∼4%.[55]

The results presented here support those obtained using Raman spectroscopy that show the structure is modified through the addition of Pr from the presence of oxygen vacancy defects. The introduction of vacancies is also likely responsible for the exhibited oxygen uptake, where the higher the vacancy concentration, the higher the oxygen uptake.

CONCLUSIONS

In this work, the presence of vacancy defects in a series of Pr−CeO_2-mixed oxides was determined to provide further insight into the oxygen uptake ability of CeO_2-based materials. Correlations between the quantities of Pr added and the oxygen uptake, Ce^{3+}, and oxygen vacancy concentration of CeO_2 were established. The materials were synthesized with Pr = 10, 15, and 20%, and the oxygen uptakes were determined as a function of % Pr and at 420 and 600 °C. The highest uptake of 95 $\mu mol \cdot g^{-1}$ was achieved for 20% Pr at 600 °C and is higher than <5 $\mu mol \cdot g^{-1}$ obtained for CeO_2. By increasing the analysis temperature, a greater portion of cations undergoes reduction to the +3 oxidation state, which, in turn, generates oxygen vacancies. The higher portion of defects acts as oxygen absorption sites to result in the increase in oxygen uptake with an increase in temperature and % Pr.

Vacancies were evident in the materials after the addition of Pr through Raman spectroscopy, as a broad defect band at 500−650 cm^{-1} was attributed to the combination of two modes because of oxygen vacancy defects and MO_8 complexes containing a Pr cation without vacancy. A downward shift in the F_{2g} mode was also attributed to the increasing quantity of oxygen vacancies, and DR UV−vis spectroscopy showed the presence of Pr^{3+}. To maintain the charge balance of the lattice, cations in the +3 oxidation state are required to accompany the oxygen vacancies.

EELS was used to qualitatively investigate the relative changes in Ce^{3+} and oxygen concentration through the calculation of the Ce I_{M_5}/I_{M_4} and O I_B/I_C ratios, respectively. The spectra of pure $PrO_{2-\delta}$ show both smaller peaks on the high-energy side because of Pr^{4+} and a shoulder peak on the lower energy side of M_4 from Pr^{3+}, implying the oxide has mixed valence. By increasing the Pr content, there was no observable increase in the Ce^{3+} concentration. The oxygen vacancy concentration was found to increase when Pr was added to CeO_2, which further increased with increasing Pr content. Thus, it was concluded that the observed oxygen uptakes of Pr−CeO_2 were due to the presence of oxygen vacancies from the addition of Pr. These results emphasize the defect nature of Pr−CeO_2 and may be used to develop materials requiring high oxygen uptakes.

ASSOCIATED CONTENT

Supporting Information

The Supporting Information is available free of charge on the ACS Publications website at DOI: 10.1021/acsomega.7b00550.

XRD pattern of the Pr−CeO_2 material with 30% Pr, STEM images of the Pr−CeO_2-mixed oxides and TEM image of $PrO_{2-\delta}$, TGA profile of $PrO_{2-\delta}$, and average EELS intensity ratios for CeO_2 and Pr−CeO_2 (PDF)

AUTHOR INFORMATION

Corresponding Author

*E-mail: alan.chaffee@monash.edu. Phone: +61 3 9905 4626 (A.L.C.).

ORCID

Anita M. D'Angelo: 0000-0002-3068-5288

Alan L. Chaffee: 0000-0001-5100-6910

Present Address

†CSIRO Mineral Resources, Private Bag 10, Clayton South, VIC, 3169, Australia.

Notes

The authors declare no competing financial interest.

ACKNOWLEDGMENTS

The authors wish to acknowledge the financial assistance provided by the Australian National Low Emissions Coal Research and Development (ANLEC R&D) and administered through the Cooperative Research Centre for Greenhouse Gas Technologies (CO2CRC). ANLEC R&D was supported by the Australian Coal Association Low Emissions Technology Limited and the Australian Government through the Clean Energy Initiative. The authors also thank the Monash Centre of Electron Microscopy. This research used the equipment funded by the Australian Research Council grant LE110100223.

REFERENCES

(1) Zheng, L. Overview of oxy-fuel combustion technology for carbon dioxide (CO_2) capture. In *Oxy-Fuel Combustion for Power Generation and Carbon Dioxide (CO_2) Capture*; Zheng, L., Ed.; Woodhead Publishing: Cambridge, 2011; pp 1−13.

(2) IPCC. *Climate Change 2014 Mitigation of Climate Change*. New York, USA, 2014.

(3) Plata, J. J.; Márquez, A. M.; Sanz, J. F. Electron mobility via polaron hopping in bulk ceria: A first-principles study. *J. Phys. Chem. C* **2013**, *117*, 14502−14509.

(4) Naik, I. K.; Tien, T. Y. Small-polaron mobility in non-stoichiometric cerium dioxide. *J. Phys. Chem. Solids* **1978**, *39*, 311−315.

(5) Su, Y.-Q.; Filot, I. A. W.; Liu, J.-X.; Tranca, I.; Hensen, E. J. M. Charge transport over the defective CeO_2(111) surface. *Chem. Mater.* **2016**, *28*, 5652−5658.

DOI: 10.1021/acsomega.7b00550
ACS Omega 2017, 2, 2544−2551

(6) Descorme, C.; Madier, Y.; Duprez, D. Infrared study of oxygen adsorption and activation on cerium−zirconium mixed oxides. *J. Catal.* **2000**, *196*, 167−173.
(7) Balaguer, M.; Yoo, C.-Y.; Bouwmeester, H. J. M.; Serra, J. M. Bulk transport and oxygen surface exchange of the mixed ionic−electronic conductor $Ce_{1-x}Tb_xO_{2-\delta}$ (x = 0.1, 0.2, 0.5). *J. Mater. Chem. A* **2013**, *1*, 10234−10242.
(8) D'Angelo, A. M.; Webster, N. A. S.; Chaffee, A. L. Vacancy generation and oxygen uptake in Cu-doped Pr-CeO_2 mixed oxides using neutron and in-situ X-ray diffraction. *Inorg. Chem.* **2016**, *55*, 12595−12602.
(9) Zhou, G.; Gorte, R. J. Thermodynamic investigation of the redox properties for ceria−hafnia, ceria−terbia, and ceria−praseodymia solid solutions. *J. Phys. Chem. B* **2008**, *112*, 9869−9875.
(10) Botu, V.; Ramprasad, R.; Mhadeshwar, A. B. Ceria in an oxygen environment: Surface phase equilibria and its descriptors. *Surf. Sci.* **2014**, *619*, 49−58.
(11) Abel, J.; Lamirand-Majimel, M.; Majimel, J.; Bellière-Baca, V.; Harlé, V.; André, G.; Prestipino, C.; Figueroa, S.; Durand, E.; Demourgues, A. Oxygen non-stoichiometry phenomena in $Pr_{1-x}Zr_xO_{2-y}$ compounds (0.02 < x < 0.5). *Dalton Trans.* **2014**, *43*, 15183−15191.
(12) Ahn, K.; Yoo, D. S.; Prasad, D. H.; Lee, H.-W.; Chung, Y.-C.; Lee, J.-H. Role of multivalent Pr in the formation and migration of oxygen vacancy in Pr-doped ceria: Experimental and first-principles investigations. *Chem. Mater.* **2012**, *24*, 4261−4267.
(13) Bishop, S. R.; Stefanik, T. S.; Tuller, H. L. Electrical conductivity and defect equilibria of $Pr_{0.1}Ce_{0.9}O_{2-\delta}$. *Phys. Chem. Chem. Phys.* **2011**, *13*, 10165−10173.
(14) Bishop, S. R.; Stefanik, T. S.; Tuller, H. L. Defects and transport in $Pr_xCe_{1-x}O_{2-\delta}$: Composition trends. *J. Mater. Res.* **2012**, *27*, 2009−2016.
(15) Chatzichristodoulou, C.; Hendriksen, P. V.; Hagen, A. Defect chemistry and thermomechanical properties of $Ce_{0.8}Pr_xTb_{0.2-x}O_{2-\delta}$. *J. Electrochem. Soc.* **2010**, *157*, B299−B307.
(16) Knauth, P.; Tuller, H. L. Nonstoichiometry and relaxation kinetics of nanocrystalline mixed praseodymium−cerium oxide $Pr_{0.7}Ce_{0.3}O_{2-x}$. *J. Eur. Ceram. Soc.* **1999**, *19*, 831−836.
(17) Chatzichristodoulou, C.; Hendriksen, P. V. Oxygen non-stoichiometry and defect chemistry modeling of $Ce_{0.8}Pr_{0.2}O_{2-\delta}$. *J. Electrochem. Soc.* **2010**, *157*, B481−B489.
(18) Reddy, B. M.; Saikia, P.; Bharali, P.; Yamada, Y.; Kobayashi, T.; Muhler, M.; Grünert, W. Structural characterization and catalytic activity of nanosized ceria−terbia solid solutions. *J. Phys. Chem. C* **2008**, *112*, 16393−16399.
(19) Niu, G.; Schubert, M. A.; d'Acapito, F.; Zoellner, M. H.; Schroeder, T.; Boscherini, F. On the local electronic and atomic structure of $Ce_{1-x}Pr_xO_{2-\delta}$ epitaxial films on Si. *J. Appl. Phys.* **2014**, *116*, 123515.
(20) Rodríguez-Luque, M. P.; Hernández, J. C.; Yeste, M. P.; Bernal, S.; Cauqui, M. A.; Pintado, J. M.; Pérez-Omil, J. A.; Stéphan, O.; Calvino, J. J.; Trasobares, S. Preparation of rhodium/$Ce_xPr_{1-x}O_2$ catalysts: A nanostructural and nanoanalytical investigation of surface modifications by transmission and scanning-transmission electron microscopy. *J. Phys. Chem. C* **2008**, *112*, 5900−5910.
(21) López-Cartes, C.; Bernal, S.; Calvino, J. J.; Cauqui, M. A.; Blanco, G.; Pérez-Omil, J. A.; Pintado, J. M.; Helveg, S.; Hansen, P. L. In situ transmission electron microscopy investigation of Ce(IV) and Pr(IV) reducibility in a Rh (1%)/$Ce_{0.8}Pr_{0.2}O_{2-x}$ catalyst. *Chem. Commun.* **2003**, 644−645.
(22) Bowman, W. J.; Zhu, J.; Sharma, R.; Crozier, P. A. Electrical conductivity and grain boundary composition of Gd-doped and Gd/Pr co-doped ceria. *Solid State Ionics* **2015**, *272*, 9−17.
(23) Bowman, W. J.; March, K.; Hernandez, C. A.; Crozier, P. A. Measuring bandgap states in individual non-stoichiometric oxide nanoparticles using monochromated STEM EELS: The Praseodymium−ceria case. *Ultramicroscopy* **2016**, *167*, 5−10.
(24) D'Angelo, A. M.; Liu, A. C. Y.; Chaffee, A. L. Oxygen uptake of Tb−CeO_2: Analysis of Ce^{3+} and oxygen vacancies. *J. Phys. Chem. C* **2016**, *120*, 14382−14389.
(25) Garvie, L. A. J.; Buseck, P. R. Determination of Ce^{4+}/Ce^{3+} in electron-beam-damaged CeO_2 by electron energy-loss spectroscopy. *J. Phys. Chem. Solids* **1999**, *60*, 1943−1947.
(26) Winterstein, J. P.; Carter, C. B. Electron-beam damage and point defects near grain boundaries in cerium oxide. *J. Eur. Ceram. Soc.* **2014**, *34*, 3007−3018.
(27) van Aken, P. A.; Liebscher, B. Quantification of ferrous/ferric ratios in minerals: new evaluation schemes of Fe L_{23} electron energy-loss near-edge spectra. *Phys. Chem. Miner.* **2002**, *29*, 188−200.
(28) ICDD. *PDF-2 2010* (Database), 2010.
(29) Mullhaupt, J. T. Process and Composition for Separation of Oxygen from Air using Pr-Ce as the Carrier. U.S. Patent Number 3980763, 1976.
(30) Wilkens, H.; Gevers, S.; Röhe, S.; Schaefer, A.; Bäumer, M.; Zoellner, M. H.; Schroeder, T.; Wollschläger, J. Structural changes of ultrathin cub-PrO_2(111)/Si(111) films due to thermally induced oxygen desorption. *J. Phys. Chem. C* **2014**, *118*, 3056−3061.
(31) Tankov, I.; Pawelec, B.; Arishtirova, K.; Damyanova, S. Structure and surface properties of praseodymium modified alumina. *Appl. Surf. Sci.* **2011**, *258*, 278−284.
(32) Li, L.; Chen, F.; Lu, J.-Q.; Luo, M.-F. Study of defect sites in $Ce_{1-x}M_xO_{2-\delta}$ (x = 0.2) solid solutions using Raman spectroscopy. *J. Phys. Chem. A* **2011**, *115*, 7972−7977.
(33) Taniguchi, T.; Watanabe, T.; Sugiyama, N.; Subramani, A. K.; Wagata, H.; Matsushita, N.; Yoshimura, M. Identifying defects in ceria-based nanocrystals by UV resonance Raman spectroscopy. *J. Phys. Chem. C* **2009**, *113*, 19789−19793.
(34) McBride, J. R.; Hass, K. C.; Poindexter, B. D.; Weber, W. H. Raman and x-ray studies of $Ce_{1-x}RE_xO_{2-y}$, where RE=La, Pr, Nd, Eu, Gd, and Tb. *J. Appl. Phys.* **1994**, *76*, 2435−2441.
(35) Shannon, R. D.; Prewitt, C. T. Effective ionic radii in oxides and fluorides. *Acta Crystallogr., Sect. B: Struct. Crystallogr. Cryst. Chem.* **1969**, *25*, 925−946.
(36) Lee, Y.; He, G.; Akey, A. J.; Si, R.; Flytzani-Stephanopoulos, M.; Herman, I. P. Raman analysis of mode softening in nanoparticle $CeO_{2-\delta}$ and Au-$CeO_{2-\delta}$ during CO oxidation. *J. Am. Chem. Soc.* **2011**, *133*, 12952−12955.
(37) Kimura, S.-i.; Arai, F.; Ikezawa, M. Mixed valence of praseodymium oxides. *J. Electron Spectrosc. Relat. Phenom.* **1996**, *78*, 135−138.
(38) Bensalem, A.; Muller, J. C.; Bozon-Verduraz, F. From bulk CeO_2 to supported cerium−oxygen clusters: A diffuse reflectance approach. *J. Chem. Soc., Faraday Trans.* **1992**, *88*, 153−154.
(39) Kasprowicz, D.; Brik, M. G.; Jaroszewski, K.; Pedzinski, T.; Bursa, B.; Głuchowski, P.; Majchrowski, A.; Michalski, E. Spectroscopic properties of $Bi_2ZnOB_2O_6$ single crystals doped with Pr^{3+} ions: Absorption and luminescence investigations. *Opt. Mater.* **2015**, *47*, 428−434.
(40) Strzęp, A.; Ryba-Romanowski, W.; Lisiecki, R.; Solarz, P.; Xu, X.; Di, J.; Xu, J. Spectroscopic peculiarities of praseodymium impurities in $Lu_3Al_5O_{12}$ single crystal. *J. Alloys Compd.* **2013**, *550*, 173−178.
(41) Kumari, L. S.; Rao, P. P.; Reddy, M. L. Environment-friendly red pigments from CeO_2−Fe_2O_3−Pr_6O_{11} solid solutions. *J. Alloys Compd.* **2008**, *461*, 509−515.
(42) Warmkessel, J. M.; Lin, S.-H.; Eyring, L. Optical absorption spectra of the ordered phases in the praseodymium oxide-oxygen system. *Inorg. Chem.* **1969**, *8*, 875−882.
(43) Kotani, A.; Mizuta, H.; Jo, T.; Parlebas, J. C. Theory of core photoemission spectra in CeO_2. *Solid State Commun.* **1985**, *53*, 805−810.
(44) Manoubi, T.; Colliex, C.; Rez, P. Quantitative electron energy loss spectroscopy on M_{45} edges in rare earth oxides. *J. Electron Spectrosc. Relat. Phenom.* **1990**, *50*, 1−18.
(45) Thole, B. T.; van der Laan, G.; Fuggle, J. C.; Sawatzky, G. A.; Karnatak, R. C.; Esteva, J.-M. 3d x-ray-absorption lines and the $3d^94f^{n+1}$ multiplets of the lanthanides. *Phys. Rev. B: Condens. Matter Mater. Phys.* **1985**, *32*, 5107−5118.

DOI: 10.1021/acsomega.7b00550
ACS Omega 2017, 2, 2544−2551

(46) Kotani, A. Core-hole effect in the Ce L_3 X-ray absorption spectra of CeO_2 and $CeFe_2$: New examination by using resonant X-ray emission spectroscopy. *Mod. Phys. Lett. B* **2013**, *27*, 1330012.
(47) Shahin, A. M.; Grandjean, F.; Long, G. J.; Schuman, T. P. Cerium L_{III}-edge XAS investigation of the structure of crystalline and amorphous cerium oxides. *Chem. Mater.* **2005**, *17*, 315−321.
(48) Braaten, N. A.; Borg, A.; Grepstad, J. K.; Raaen, S.; Ruckman, M. W. Oxygen K near-edge-structure for thin Ce oxide films. *Solid State Commun.* **1991**, *77*, 731−734.
(49) Kanoun, M. B.; Reshak, A. H.; Kanoun-Bouayed, N.; Goumri-Said, S. Evidence of Coulomb correction and spin−orbit coupling in rare-earth dioxides CeO_2, PrO_2 and TbO_2: An ab initio study. *J. Magn. Magn. Mater.* **2012**, *324*, 1397−1405.
(50) Herrero-Martín, J.; García-Muñoz, J. L.; Valencia, S.; Frontera, C.; Blasco, J.; Barón-González, A. J.; Subías, G.; Abrudan, R.; Radu, F.; Dudzik, E.; et al. Valence change of praseodymium in $Pr_{0.5}Ca_{0.5}CoO_3$ investigated by x-ray absorption spectroscopy. *Phys. Rev. B: Condens. Matter Mater. Phys.* **2011**, *84*, 115131.
(51) Mullins, D. R.; Overbury, S. H.; Huntley, D. R. Electron spectroscopy of single crystal and polycrystalline cerium oxide surfaces. *Surf. Sci.* **1998**, *409*, 307−319.
(52) Tang, Y.; Zhang, H.; Cui, L.; Ouyang, C.; Shi, S.; Tang, W.; Li, H.; Lee, J.-S.; Chen, L. First-principles investigation on redox properties of M-doped CeO_2 (M=Mn, Pr, Sn, Zr). *Phys. Rev. B: Condens. Matter Mater. Phys.* **2010**, *82*, 125104.
(53) Dileep, K.; Panchakarla, L. S.; Balasubramanian, K.; Waghmare, U. V.; Datta, R. Electron energy loss spectroscopy of ZnO nanocrystals with different oxygen vacancy concentrations. *J. Appl. Phys.* **2011**, *109*, 063523.
(54) Chen, S.-Y.; Chen, R.-J.; Lee, W.; Dong, C.-L.; Gloter, A. Spectromicroscopic evidence of interstitial and substitutional dopants in association with oxygen vacancies in Sm-doped ceria nanoparticles. *Phys. Chem. Chem. Phys.* **2014**, *16*, 3274−3281.
(55) Muller, D. A.; Nakagawa, N.; Ohtomo, A.; Grazul, J. L.; Hwang, H. Y. Atomic-scale imaging of nanoengineered oxygen vacancy profiles in $SrTiO_3$. *Nature* **2004**, *430*, 657−661.

DOI: 10.1021/acsomega.7b00550
ACS Omega 2017, 2, 2544−2551